Int. J. Heat Mass Transfer. Vol. 34, No. 9, pp. 2389–2349, 1991
Printed in Great Britain

0017–9310/91 $3.00+0.00

Analysis of passive cooling in a vertical finite channel using a falling liquid film and buoyancy-induced gas–vapor flow

H. CHIANG and C. KLEINSTREUER†

Department of Mechanical and Aerospace Engineering, North Carolina State University, Raleigh, NC 27695-7910, U.S.A.

(*Received* 5 *March* 1990 *and in final form* 30 *October* 1990)

Abstract—A fundamental study of the coupled effects of a falling, partially vaporizing liquid film and buoyancy-induced gas–vapor flow in a vertical one-sided heated channel is presented for different film Reynolds numbers, liquid film inlet temperatures, wall heat fluxes and channel spacings. The transient (elliptic) gas-phase transport equations are solved numerically in conjunction with the laminar (parabolic) liquid film equations. The validated computer simulation model is used to depict transient developments of streamlines, gas-phase parameters and interfacial quantities as well as steady-state velocity profiles, temperature profiles and averaged Nusselt number distributions. The present analysis may contribute to the solution of passive cooling problems associated with electronic equipment operations, manufacturing processes, modern nuclear power plant designs and numerous environmental phenomena.

1. INTRODUCTION

PASSIVE cooling, utilizing the combined heat/mass transfer process of a falling liquid film, liquid heating and evaporation, and buoyant gas–vapor flow, is a reliable way to prevent excessive temperature build-up in many engineering and natural systems. Of interest in this paper is transient two-dimensional laminar convection of an air–vapor mixture interacting with a steady smooth water film in a vertical channel of finite length (cf. Fig. 1). One channel side is heated (q_w = const.) and the other side is insulated. The film temperature increases with time and varies in space due to the constant wall heat flux and the changing interfacial heat/mass transfer. The heat and mass diffusions between the liquid and the gas generate density variations in the gas region which induce natural convection. If the buoyancy forces are strong enough to overcome the drag force of the falling film, a counter-current gas–vapor flow is formed, resulting in a reliable mode of passive cooling. Applications of such natural cooling systems can be found in electronic equipment operations, manufacturing processes, modern nuclear power plant designs and in numerous environmental phenomena.

Previous studies focused on single aspects of the present analysis. For example, Chang and Lin [1] investigated numerically transient natural convection in a symmetrically heated vertical channel of finite height. They observed the temporal evolution of multiple cells in the channel which are highly dependent upon the channel exit effects. Natural convection inside a one-sided heated vertical channel was experimentally and theoretically analyzed by Sparrow *et al.* [2]. They [2, 3] developed Nusselt number correlations for a practical range of Rayleigh numbers and interplate spacings. The combined buoyancy effects due to temperature differences and concentration differences were investigated by Chang *et al.* [4] for a vertical wetted tube and by Gebhart and Pera [5] for a vertical flat plate. Their results indicate that the two independent but additive buoyancy forces enhance natural convection and, in case of air–water vapor mixtures, may improve the overall cooling effect significantly. Experimental and a few numerical studies of falling liquid films under various operational conditions have been conducted by numerous investigators [6–12]. For example, Cerza and Sernas [7] considered falling film cooling of a nuclear reactor and Gorla and Maloney [8] analyzed falling film cooling of a fin surface. In these previous works mass diffusion was neglected assuming that the liquid film was surrounded by its own stagnant vapor with the saturation temperature at the liquid–gas interface. Thus, the present paper illustrates the combined effects of mass diffusion and natural convection on passive cooling using a falling film.

2. ANALYSIS

Figure 1 depicts the system schematics with appropriate coordinates as well as the computational domain. Two large reservoirs are included in order to simulate channel exit effects and to provide simple gas inflow and outflow conditions for the elliptic-type differential equations (cf. ref. [1]). Key assumptions for this liquid film/gas–vapor flow system are listed and justified in Table 1.

† Author to whom all correspondence should be addressed.

NOMENCLATURE

A	aspect ratio, H/S
c	reduced factor in computational domain, $c \leqslant 1$
D	mass diffusivity
g	gravitational acceleration constant
Gr_T	Grashof number of thermal diffusion
Gr_M	Grashof number of mass diffusion
H	channel height
$\bar{h}$	height-averaged heat transfer coefficient, $q_w/(\bar{T}_w - \bar{T}_i)$
h_{fg}	latent heat of evaporation
k	thermal conductivity
M	molecular weight
$\overline{Nu}_f$	liquid film Nusselt number, $\bar{h}(v_1^2/g)^{1/3}/k_1$
$\overline{Nu}_g$	gas-phase Nusselt number, $\bar{q}_i/(\bar{T}_i - \bar{T}_{y=S})(S/k_2)$
P	dimensionless dynamic pressure
Pe	Peclet number
Pr	Prandtl number, v/α
p	total absolute pressure
p_d	hydraulically dynamic pressure
p_v	saturated vapor pressure at the interface temperature
Q_g	gas-phase volumetric flow rate
q_w	wall heat flux
q_i	total interfacial heat fluxes
q_c	sensible heat due to temperature gradient
q_d	latent heat due to vapor concentration gradient
Ra_S	Rayleigh number based on channel spacing
Ra_H	Rayleigh number based on channel height
Re	Reynolds number
Re_f	liquid film Reynolds number
S	channel spacing
Sc	Schmidt number
T	temperature
T_0	ambient temperature
T_r	inlet water temperature
T_w	heated wall temperature
t	time
U	dimensionless longitudinal velocity
u	longitudinal velocity
V	dimensionless transversal velocity
v	transversal velocity
W	dimensionless vapor mass fraction
X	dimensionless longitudinal coordinate
x	longitudinal coordinate
Y	dimensionless transversal coordinate
y	transversal coordinate.

Greek symbols

α	thermal diffusivity
β	thermal expansion coefficient
β^*	expansion coefficient for concentration variation
Γ	film mass flow rate per unit perimeter
γ	dimensionless film thickness
δ	liquid film thickness
ε	dimensionless interfacial shear stress
η	dimensionless coordinate, $Y_2 - 1/2$
θ	dimensionless temperature
μ	dynamic viscosity
ν	kinematic viscosity
ξ	dimensionless coordinate, $X_2 - A/2$
ρ	density
τ	dimensionless time
τ_i	interfacial shear stress
ϕ	pressure correction factor
ϕ_{H0}	relative humidity at ambient condition
ω	mass fraction of vapor.

Subscripts

0	at ambient condition
1, f	liquid (water)
2, g	gas (air and water vapor)
a	diffusion species
b	carrier fluid
c	convection
d	diffusion; dynamic
i	interface
r	at water inlet condition
S	channel spacing
v	vapor
w	wall.

2.1. *Falling liquid film*

Since the interfacial shear stress τ_i is very small, a quasi-steady fully-developed liquid film velocity profile is assumed [9]

$$u_1 = \frac{\phi g}{\nu_1}\left[\left(\delta - \frac{\tau_i}{\rho_1 g \phi}\right) y_1 - \frac{y_1^2}{2}\right] \tag{1}$$

where $\delta = \delta(x_1)$ and $\phi = 1 - (1/g\rho_1)(\partial p/\partial x_1)$. Neglecting axial heat conduction inside the thin falling film, the quasi-steady heat equation reads

$$u_1 \frac{\partial T_1}{\partial x_1} = \alpha_1 \frac{\partial^2 T_1}{\partial y_1^2} \tag{2}$$

$$T = T_r \qquad \text{at } x_1 = 0 \tag{3a}$$

$$-k_1 \frac{\partial T_1}{\partial y_1} = q_w = \text{constant} \qquad \text{at } y_1 = 0 \tag{3b}$$

and

$$-k_1 \frac{\partial T_1}{\partial y_1} = q_i(x_1) \qquad \text{at } y_1 = \delta(x_1). \tag{3c}$$

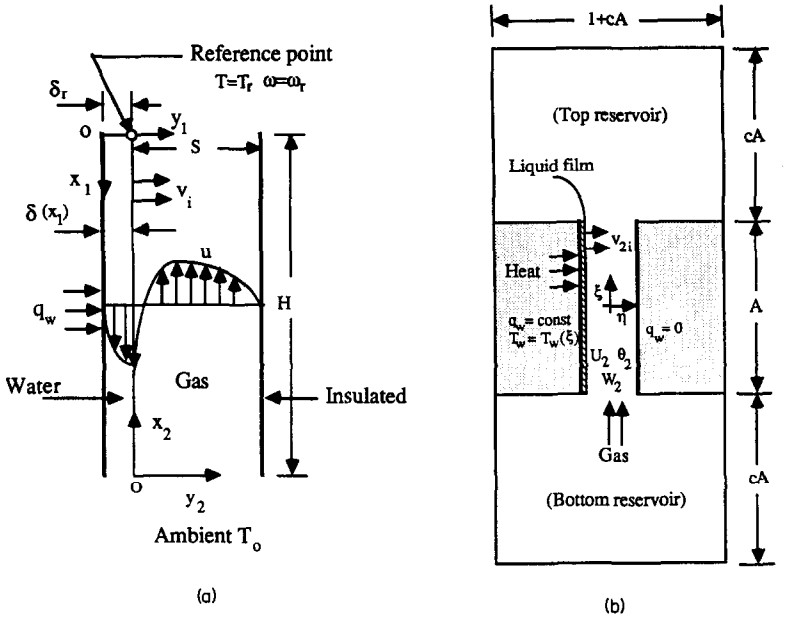

FIG. 1. System schematics and computational domain.

In terms of the dimensionless variables $U_1 = u_1/u_{ref}$, $\theta_1 = (T_1 - T_r)/(q_w\delta_r/k_1)$, $X_1 = x_1/S$ and $Y_1 = y_1/\delta_r$, equations (1)–(3) can be rewritten as

$$U_1 = 2(\gamma - \varepsilon)Y_1 - Y_1^2 \tag{4}$$

$$U_1\frac{\partial\theta_1}{\partial X_1} = \frac{1}{Pe_1}\left(\frac{S}{\delta_r}\right)\frac{\partial^2\theta_1}{\partial Y_1^2} \tag{5}$$

and

$$\theta_1(X_1 = 0) = 0 \tag{6a}$$

$$\left.\frac{\partial\theta_1}{\partial Y_1}\right|_{Y_1=0} = -1 \tag{6b}$$

and

$$\left.\frac{\partial\theta_1}{\partial Y_1}\right|_{Y_1=\gamma} = \frac{q_c}{q_w} + \frac{q_d}{q_w}. \tag{6c}$$

Here, $u_{ref} = \rho_1 g\delta_r^2/(2\mu_1)$, $\gamma = \delta/\delta_r$ and $\varepsilon = \tau_i/(\rho_1 g\phi\delta_r)$. The reference velocity, $u_{ref} = u_1(y_1 = \delta_r;\ \varepsilon \equiv 0)$, can be used to calculate the film mass flow rate per unit perimeter at the inlet (reference point r), namely

$$\Gamma_r = \int_0^{\delta_r}\rho_1 u_1\,dy_1 = \rho_1 u_{ref}\delta_r(2/3 - \varepsilon) \tag{7}$$

and hence the film Reynolds number

$$Re_f = \frac{4\Gamma_r}{\mu_1} = 4Re_1(2/3 - \varepsilon) \tag{8}$$

where $Re_1 = u_{ref}\delta_r/\nu_1$.

2.2. *Gas region*

Assuming transient laminar, basically incompressible two-dimensional air–water vapor flow, the governing equations for the gas region are:

continuity

$$\frac{\partial u_2}{\partial x_2} + \frac{\partial v_2}{\partial y_2} = 0 \tag{9}$$

Table 1. Critical parameter values for gravity film and buoyancy-induced gas flow assumptions

Assumptions	Critical values	[refs.]	Data used	Comments
Laminar liquid film	$Re_f \leqslant 1500$	[11]	$10 \leqslant Re_f \leqslant 200$	—
No film break-up	$\delta \geqslant 0.1$ mm	[10]	$\delta_{min} = 0.07$ mm	no initial dry spots as assumed in ref. [10]
No nucleate boiling	$q_w \leqslant 8$ kW m^{-2}	[7]	$q_w \leqslant 5$ kW m^{-2}	—
Laminar gas flow	$Ra_H \leqslant 10^9$	[2]	$Ra_H \leqslant 10^7$	—

Note: Properties of the liquid film are evaluated at $T = 50$°C.

momentum

$$\rho_2\left(\frac{\partial u_2}{\partial t}+u_2\frac{\partial u_2}{\partial x_2}+v_2\frac{\partial u_2}{\partial y_2}\right)= -\frac{\partial p}{\partial x_2}+\mu_2\left(\frac{\partial^2 u_2}{\partial x_2^2}+\frac{\partial^2 u_2}{\partial y_2^2}\right)-\rho_2 g \quad (10)$$

$$\rho_2\left(\frac{\partial v_2}{\partial t}+u_2\frac{\partial v_2}{\partial x_2}+v_2\frac{\partial v_2}{\partial y_2}\right)= -\frac{\partial p}{\partial y_2}+\mu_2\left(\frac{\partial^2 v_2}{\partial x_2^2}+\frac{\partial^2 v_2}{\partial y_2^2}\right) \quad (11)$$

energy

$$\frac{\partial T_2}{\partial t}+u_2\frac{\partial T_2}{\partial x_2}+v_2\frac{\partial T_2}{\partial y_2}=\alpha_2\left(\frac{\partial^2 T_2}{\partial x_2^2}+\frac{\partial^2 T_2}{\partial y_2^2}\right) \quad (12)$$

mass diffusion

$$\frac{\partial \omega_2}{\partial t}+u_2\frac{\partial \omega_2}{\partial x_2}+v_2\frac{\partial \omega_2}{\partial y_2}=D_2\left(\frac{\partial^2 \omega_2}{\partial x_2^2}+\frac{\partial^2 \omega_2}{\partial y_2^2}\right) \quad (13)$$

subject to the initial condition for $t=0$

$$u_2=v_2=0, \quad T_2=T_0 \quad \text{and} \quad \omega_2=\omega_0 \quad (14)$$

and the boundary conditions for $t>0$

$$u_2=u_i, \quad v_2=v_i,$$

$$T_2=T_i \quad \text{and} \quad \omega_2=\omega_i \quad \text{at } y_2=0 \quad (15)$$

and

$$u_2=v_2=0 \quad \text{and} \quad \frac{\partial T_2}{\partial y_2}=\frac{\partial \omega_2}{\partial y_2}=0 \quad \text{at } y_2=S. \quad (16)$$

The Boussinesq approximation can be applied to express the buoyancy effects due to small gas density variations caused by thermal expansion and vapor diffusion. Thus following the experimental results given by Gebhart and Pera [5]

$$\rho_2=\rho_0[1-\beta(T_2-T_0) -\beta^*(\omega_2-\omega_0)+\mathcal{O}(\Delta T_2^2,\Delta\omega_2^2)] \quad (17)$$

where $\beta=1/T_0$ and $\beta^*=-(1-M_b/M_a)$ so that with $p=p_d+p_0-\rho_0 g x$, the pressure gradients in equations (10) and (11) can be written as

$$\frac{\partial p}{\partial x_2}=\frac{\partial p_d}{\partial x_2}-\rho_0 g \quad \text{and} \quad \frac{\partial p}{\partial y_2}=\frac{\partial p_d}{\partial y_2}. \quad (18a, b)$$

At the gas–liquid interface, the liquid film equations and the gas-phase equations are coupled via boundary conditions (15). While the values for u_i and T_i are evaluated from equations (1) and (2), the interfacial vapor concentration and blowing velocity can be calculated after the temperature at the liquid–gas interface is known, namely

$$\omega_i=\frac{M_a p_v}{M_a p_v+M_b(p-p_v)} \quad (19)$$

$$v_i=-\frac{D_2}{1-\omega_i}\frac{\partial \omega_2}{\partial y_2}\bigg|_{y_2=0} \quad (20)$$

where p and p_v are the local absolute pressure and the vapor pressure at the interface, respectively. By assuming that the interface is in thermodynamic equilibrium, the relation between the saturated temperature and saturated pressure is described by the Clausius–Clapeyron equation. A convenient set of correlations programmed here for calculating the saturated pressure and latent heat at a specified saturated temperature was developed by Irvine and Liley [13]. The heat transfer at the liquid–gas interface can be expressed as

$$q_i=q_c+q_d=-k_2\frac{\partial T_2}{\partial y_2}\bigg|_{y_2=0}+\rho_2 v_i h_{fg} \quad (21)$$

and computed after solving the gas-phase equations.

Using the following dimensionless variables:

$$X_2=\frac{x_2}{S}, \quad Y_2=\frac{y_2}{S}, \quad \tau=\frac{\nu_2 t}{S^2}$$

$$U_2=\frac{u_2 S}{\nu_2}, \quad V_2=\frac{v_2 S}{\nu_2}, \quad P=p_d\left(\frac{S^2}{\rho_2\nu_2^2}\right)$$

$$\theta_2=\frac{T_2-T_0}{T_r-T_0} \quad \text{and} \quad W_2=\frac{\omega_2-\omega_0}{\omega_r-\omega_0} \quad (22)$$

the gas-phase equations (9)–(13) subject to equations (14)–(18) can be rewritten as

$$\frac{\partial U_2}{\partial X_2}+\frac{\partial V_2}{\partial Y_2}=0 \quad (23)$$

$$\frac{\partial U_2}{\partial \tau}+U_2\frac{\partial U_2}{\partial X_2}+V_2\frac{\partial U_2}{\partial Y_2}=-\frac{\partial P}{\partial X_2} +\left(\frac{\partial^2 U_2}{\partial X_2^2}+\frac{\partial^2 U_2}{\partial Y_2^2}\right)+Gr_T\theta_2+Gr_M W_2 \quad (24)$$

$$\frac{\partial V_2}{\partial \tau}+U_2\frac{\partial V_2}{\partial X_2}+V_2\frac{\partial V_2}{\partial Y_2}= -\frac{\partial P}{\partial Y_2}+\left(\frac{\partial^2 V_2}{\partial X_2^2}+\frac{\partial^2 V_2}{\partial Y_2^2}\right) \quad (25)$$

$$\frac{\partial \theta_2}{\partial \tau}+U_2\frac{\partial \theta_2}{\partial X_2}+V_2\frac{\partial \theta_2}{\partial Y_2}=\frac{1}{Pr_2}\left(\frac{\partial^2\theta_2}{\partial X_2^2}+\frac{\partial^2\theta_2}{\partial Y_2^2}\right) \quad (26)$$

and

$$\frac{\partial W_2}{\partial \tau}+U_2\frac{\partial W_2}{\partial X_2} +V_2\frac{\partial W_2}{\partial Y_2}=\frac{1}{Sc_2}\left(\frac{\partial^2 W_2}{\partial X_2^2}+\frac{\partial^2 W_2}{\partial Y_2^2}\right). \quad (27)$$

Here, the Grashof number of thermal diffusion Gr_T

and the Grashof number of mass diffusion Gr_M are defined as

$$Gr_T = \frac{g\beta(T_r - T_0)S^3}{\nu_2^2} \quad \text{and} \quad Gr_M = \frac{g\beta^*(\omega_r - \omega_0)S^3}{\nu_2^2} \tag{28a, b}$$

respectively. The initial conditions for the gas region are

$$U_2 = V_2 = \theta_2 = W_2 = 0 \quad \tau \leqslant 0. \tag{29}$$

The boundary conditions at the insulated wall are

$$U_2 = V_2 = 0, \quad \frac{\partial \theta_2}{\partial Y_2} = \frac{\partial W_2}{\partial Y_2} = 0 \quad \text{at } Y_2 = 1, \quad \tau > 0. \tag{30}$$

The boundary conditions at the liquid–gas interface ($Y_2 = 0$) have to match the solution of the liquid region, and they have the following forms:

$$U_{2i} = Re_2 U_{1i}, \quad Re_2 = \frac{u_{ref} S}{\nu_2} \tag{31a, b}$$

$$V_{2i} = -\frac{\omega_r - \omega_0}{(1-\omega_i)} \frac{1}{Sc_2} \left(\frac{\partial W_2}{\partial Y_2}\right)_i \tag{32}$$

$$\theta_{2i} = \frac{q_w}{k_1 \dfrac{T_r - T_0}{\delta_r}} \theta_{1i} + 1 \tag{33}$$

and

$$W_{2i} = \frac{\omega_i - \omega_0}{\omega_r - \omega_0}. \tag{34}$$

Now, the compatibility condition (21) can be expressed as

$$\frac{\partial \theta_1}{\partial Y_1} = \frac{q_c}{q_w} + \frac{q_d}{q_w} = \frac{1}{q_w}\left[k_2 \frac{T_r - T_0}{S} \frac{\partial \theta_2}{\partial Y_2} + \frac{\rho_2 D_2 h_{fg}}{(1-\omega_i)} \frac{\omega_r - \omega_0}{S} \frac{\partial W_2}{\partial Y_2}\right] \quad \text{for } Y_1 = \delta/\delta_r. \tag{35}$$

Since the boundary conditions at the channel entrance and channel exit are not known a priori, two large reservoirs are attached (cf. Fig. 1) with the conditions of zero normal velocity gradients and zero tangential velocity components on the control surfaces of these reservoirs. Numerical experiments [1] indicated that these infinite domains can be replaced by reservoirs of finite size, i.e. $0.5 \leqslant c \leqslant 1.0$, assuming a narrow channel and fully-developed flow boundary conditions.

3. NUMERICAL ANALYSIS

Since the liquid film velocity profile is known, the parabolic energy equation (5) can be directly solved with a simple marching-type finite difference scheme. The compatibility conditions for τ_i, T_i and q_i at the interface couple iteratively the liquid film with the gas–vapor region. An elliptic equation solver 'SIMPLE' described by Patankar [14] is employed to solve the transient two-dimensional gas-phase equations (23)–(27). The control volume formulation of this algorithm ensures conservation of momentum, mass and energy and its interface integral feature provides a better convergence capability in dealing with nonlinear boundary or compatibility conditions. A two-dimensional mesh of varying density was developed via trial and error in order to: (i) resolve the boundary layer (cf. $\delta/S \sim Ra_S^{-1/4}$ from scale analysis), (ii) have finer meshes near the interface, along the walls and in the channel inlet/exit areas, and (iii) achieve mesh-independent results as well as a computationally efficient code. The numerical solution procedure is depicted in Fig. 2.

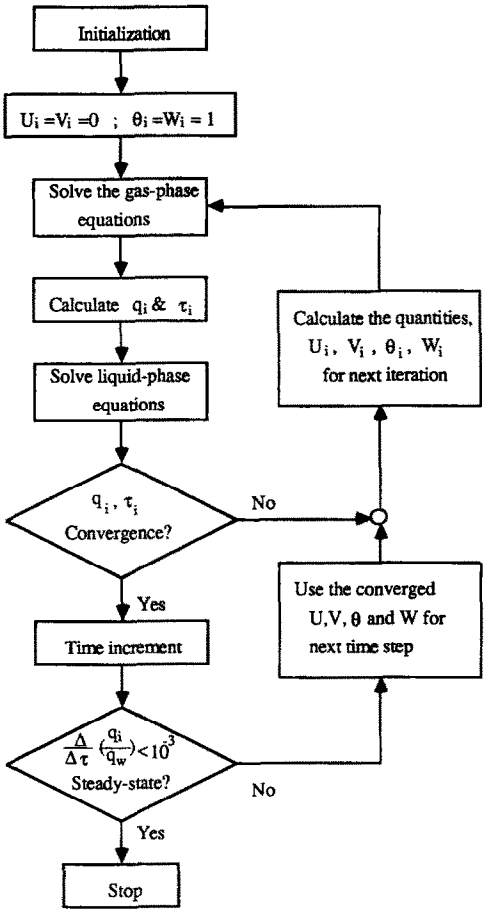

FIG. 2. Computational flow chart.

4. RESULTS AND DISCUSSION

4.1. *Model validation*

Because of the absence of experimental data for unsteady flow of a liquid falling film evaporating into an unsaturated buoyant gas stream, the present computer simulation model has been validated by com-

Table 2. Comparison of model predictions with measured Nusselt numbers given by Sparrow *et al.* [2]

H/S	Ra_S	Nusselt number: Sparrow *et al.* [2]	Nusselt number: Present work
15.24	9.14×10^3	3.38	3.46
15.24	4.26×10^4	4.96	4.97
11.42	9.75×10^4	6.55	6.63
11.42	4.57×10^5	9.63	9.12

parisons with special case studies [1, 2]. First the transient, buoyancy-induced flow patterns in a finite vertical channel with non-evaporating surfaces (cf. ref. [1]) were exactly reproduced, and then fluid flow reversal in a one-sided heated vertical channel, experimentally observed by Sparrow *et al.* [2], was successfully simulated. A comparison of predicted vs measured Nusselt numbers is given in Table 2.

4.2. *Transient flow results*

Typical input data sets for Figs. 3–9 are summarized in Table 3. With the given operational parameters, the transient period of this problem lasts about 1 min. The temporal gas flow developments for a film Reynolds number of $Re_f = 30$ are depicted in terms of stream function contours in Figs. 3(a)–(c); only portions of the inlet/outlet reservoirs are shown. In the incipient moment ($\tau = 0.0022$), the interactions of film drag-induced gas flow, blowing due to water evaporation and free convection of the air–vapor mixture generate two flow regions, one upward and one downward (cf. Fig. 3(a)). At $\tau = 0.05$, the interfacial drag has set up a distinct recirculation zone, pulling 'cold' air into the channel from the top reservoir and discharging it at the bottom (cf. Fig. 3(b)). As time progresses, $\tau = 0.5$, the air–vapor mixture heats up and the buoyancy forces dominate over the drag force, causing a very thin recirculation zone along the gas–liquid interface and rather uniform natural convection elsewhere in the channel (cf. Fig. 3(c)). It has to be noted that the recirculation zone is too thin to show up on Fig. 3(c); however, Figs. 5(a)–(c) indicate that a thin recirculation layer exists along the wall. Inside the top reservoir, the strong gas flow generates two vortices which vanish when steady state is reached, i.e. at $\tau \approx 1.0$. One can conclude from the transient flow field developments that there is a higher heat transfer rate at the early stage when the liquid film is contacting the cold air and the interfacial (blowing) velocity is high (cf. Fig. 4). After $\tau \approx 0.4$ a slight increase in V_{2i} can be observed because of the increase in natural gas convection, reducing the gas-phase water vapor concentration. The thin long recirculation zone near the interface may block cold air off the falling film and subsequently decreases the heat transfer.

The sequence of axial velocity profiles, Figs. 5(a)–(c), is complementary to the streamline contours shown in Figs. 3(a)–(c). Initially $\tau = 0.0022$, flow in the entire region of interest is downwards in the lower part of the channel (cf. Fig. 5(a)) and upwards, except the film and a gas layer at the interface, in the upper part of the channel (cf. Fig. 5(c)). The thickness of the drag-induced gas layer at the interface first increases and is then reduced due to the increasing buoyancy effects.

4.3. *Steady-state heat/mass transfer results*

Figures 6(a) and (b) show the interfacial heat flux and the wall temperature profiles, respectively, for various film Reynolds numbers. The heat flux is caused by both temperature and vapor concentration gradients with the latent heat transfer (cf. q_i in equation (21) or (35)) being the dominant mechanism

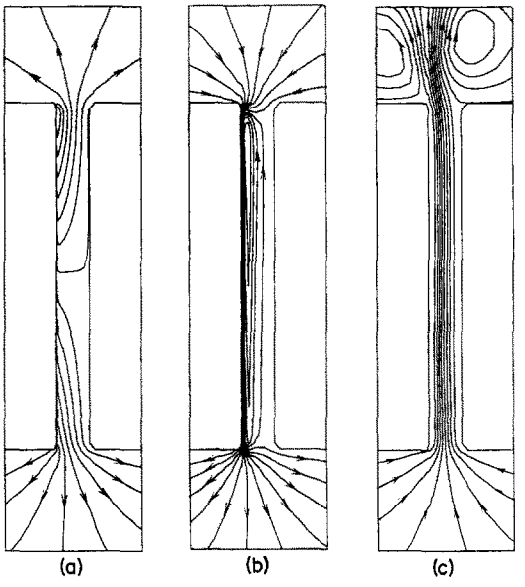

FIGS. 3(a)–(c). Transient development of stream functions at $\tau = 0.0022$, 0.05 and 0.5 ($Re_f = 30$, $q_w = 1$ kW m^{-2}, $T_r = 35$°C, $S = 0.01$ m).

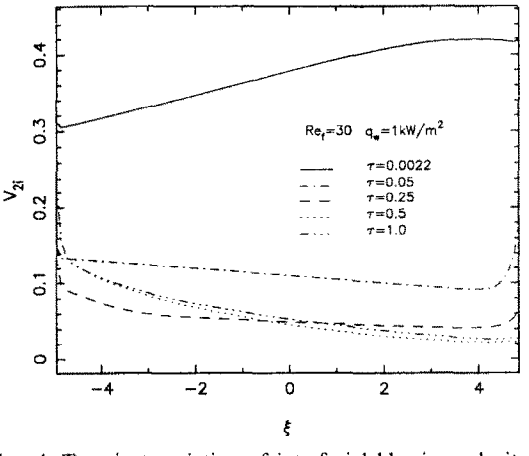

FIG. 4. Transient variation of interfacial blowing velocity ($Re_f = 30$, $q_w = 1$ kW m^{-2}, $T_r = 35$°C, $S = 0.01$ m).

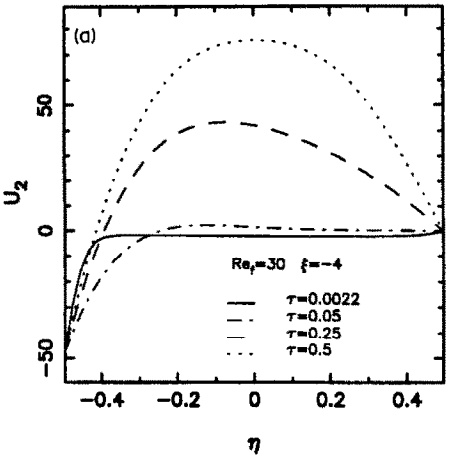

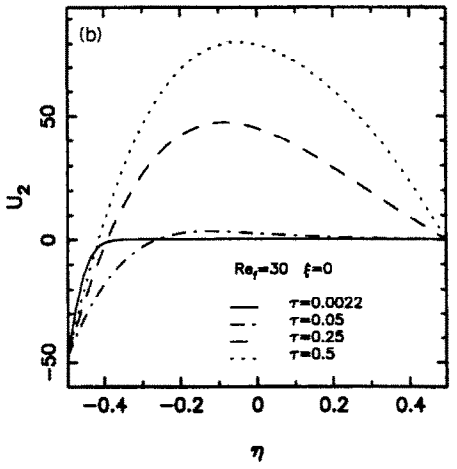

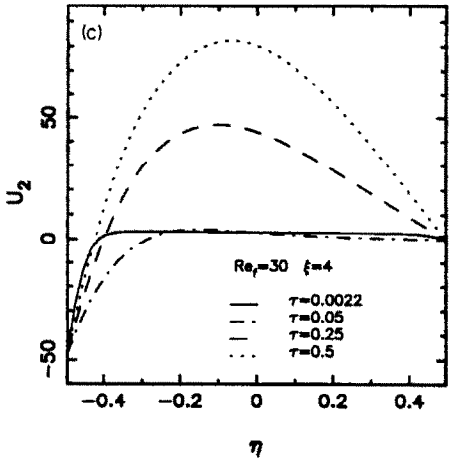

FIGS. 5(a)–(c). Transient variations of axial velocity profiles near channel bottom ($\xi = -4$), at channel center ($\xi = 0$) and near channel exit ($\xi = 4$) ($Re_f = 30$, $q_w = 1$ kW m^{-2}, $T_r = 35$°C, $S = 0.01$ m).

which indicates a strong deviation from the classical Nusselt problem where $q_i = q_w$. At low Reynolds numbers, e.g. $Re_f \approx 10$, the interfacial heat flux may exceed the wall heat flux near the channel exit because of the (convective) evaporation cooling effect (cf. Fig. 6(a)). This, in turn, affects the wall temperature very positively (cf. Fig. 6(b)). At higher film Reynolds numbers, say $Re_f = 200$, the drag-induced recirculation layer, which acts like a buffer zone between the liquid film and the buoyant gas mixture, is quite thick ($\approx 0.35S$) and shifted downwards into the bottom reservoir. As a result, q_i is rather uniform for $-5 \leqslant \xi \leqslant 3$ and then increases sharply because of the strong interfacial gradients near the top part of the channel.

The coupled momentum, heat and mass transfer in

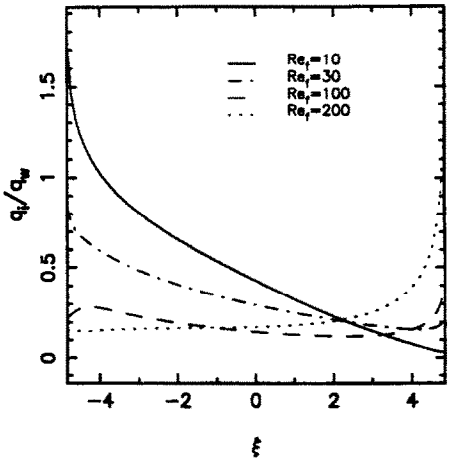

FIG. 6(a). Variation of relative interfacial heat fluxes at several film Reynolds numbers ($Re_f = 10$, 30, 100 and 200, $q_w = 1$ kW m^{-2}, $T_r = 35$°C, $S = 0.01$ m).

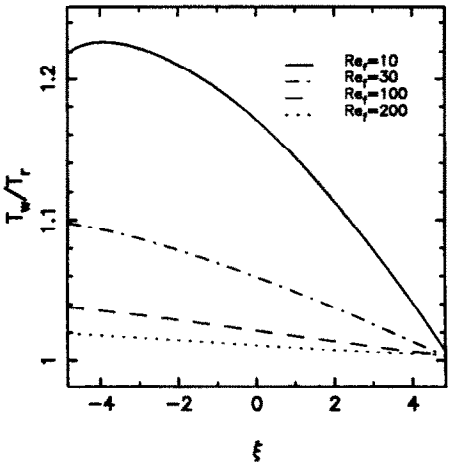

FIG. 6(b). Variation of relative wall temperatures at several film Reynolds numbers ($Re_f = 10$, 30, 100 and 200, $q_w = 1$ kW m^{-2}, $T_r = 35$°C, $S = 0.01$ m).

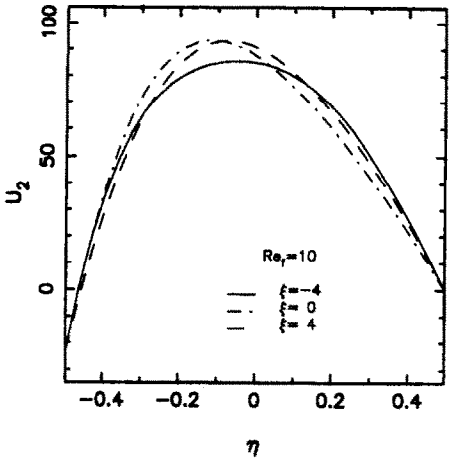

FIG. 7(a). Longitudinal velocity profiles at three different channel locations, $\xi = -4$, 0 and 4 ($Re_f = 10$, $q_w = 1$ kW m^{-2}, $T_r = 35$°C, $S = 0.01$ m).

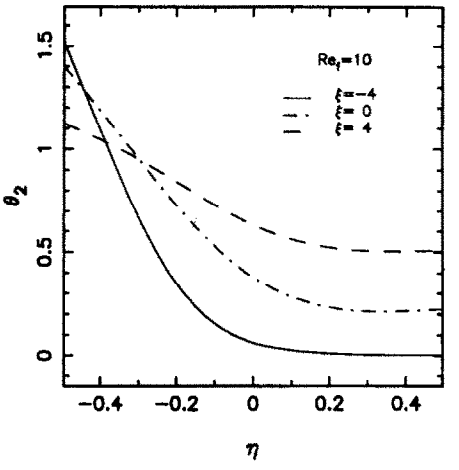

FIG. 7(b). Temperature profiles at three different channel locations, $\xi = -4$, 0 and 4 ($Re_f = 10$, $q_w = 1$ kW m^{-2}, $T_r = 35$°C, $S = 0.01$ m).

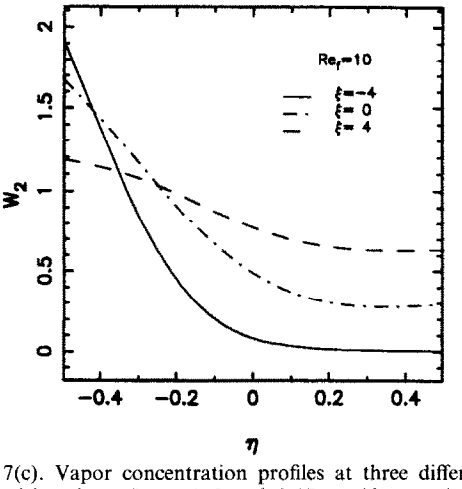

FIG. 7(c). Vapor concentration profiles at three different channel locations, $\xi = -4$, 0 and 4 ($Re_f = 10$, $q_w = 1$ kW m^{-2}, $T_r = 35$°C, $S = 0.01$ m).

the gas region is depicted in Figs. 7(a)–(c) for $Re_f = 10$. The axial velocity profile increases and shifts due to changing buoyancy forces along the channel length (cf. Figs. 7(a) and 6(a)). The thermal and vapor-concentration boundary layer thicknesses (or penetration depths) can be deduced from Figs. 7(b) and (c), respectively. The rather flat profiles $\theta_2(\eta)$ and $W_2(\eta)$ in the upper portion of the channel indicate that the effects of interfacial heat and mass transfer rates have diminished and the exit gas–vapor mixture is more uniform.

4.4. *Averaged heat flux and Nusselt number distributions*

Figures 8(a), (b) and 9(a), (b) show the effects of different system parameters on channel width-averaged or height-averaged gas-phase and liquid-phase quantities. Dimensionless net gas flow rates

$$Q_g/v_g = \int_0^1 U_2 \, dY_2$$

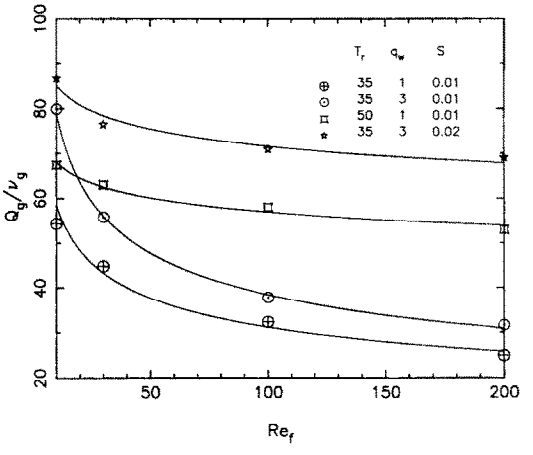

FIG. 8(a). Dimensionless gas-phase volumetric flow rate as a function of film Reynolds number for different wall heat fluxes, liquid inlet temperatures and channel spacings.

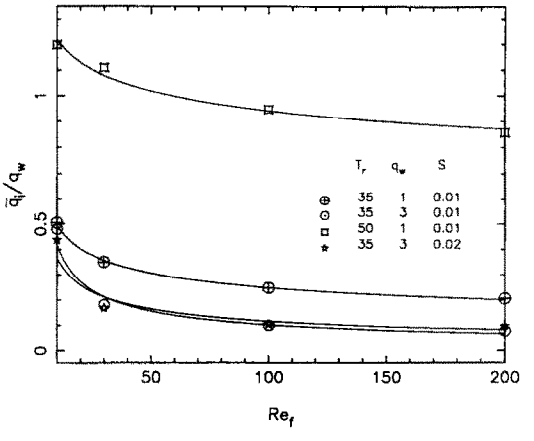

FIG. 8(b). Averaged relative interfacial heat flux as a function of film Reynolds number for different wall heat fluxes, liquid inlet temperatures and channel spacings.

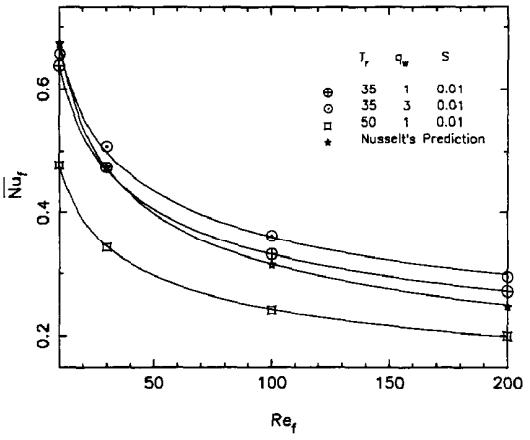

FIG. 9(a). Film Nusselt number variations as a function of Reynolds number for different wall heat fluxes and liquid inlet temperatures.

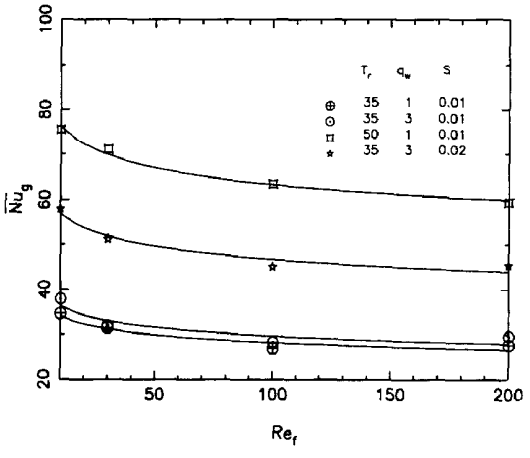

FIG. 9(b). Gas phase Nusselt number variations as a function of film Reynolds number for different wall heat fluxes, liquid inlet temperatures and channel spacings.

evaluated at $\xi = 0$, as a function of film Reynolds number are given in Fig. 8(a). As expected, higher inlet water temperatures ($T_r = 50°C$) induce larger interfacial temperature and concentration gradients and hence stronger buoyancy-driven gas flows weakly dependent upon the film Reynolds number. Similar trends are apparent for a lower film temperature ($T_r = 35°C$) but a larger wall heat flux ($q_w = 3$ kW m^{-2}) and wider spacing ($S = 0.02$ m) mainly because of the higher interfacial temperature and the reduced frictional effect of the falling film. The dependence of the buoyant gas flow on the film Reynolds number is stronger for small channel spacings ($S = 0.01$ m) and relatively low water film temperatures ($T_r = 35°C$). Figure 8(b) depicts the height-averaged interfacial heat flux $\bar{q}_i$ which consists of the latent heat for liquid vaporization and the sensible heat for gas-phase heating. Thus, the difference $(1 - \bar{q}_i/q_w)$ is utilized for liquid film heating or cooling depending upon T_r. For example, a high water inlet temperature ($T_r = 50°C$) results in high interfacial heat fluxes, exceeding the wall heat flux at low Reynolds numbers ($Re_f \leqslant 60$). At a higher wall heat flux ($q_w = 3$ kW m^{-2}) and a lower T_r ($T_r = 35°C$), the heat flux ratio $\bar{q}_i/q_w$ is basically independent of the channel width because larger spacings generate smaller gas velocities but also larger recirculation zones which diminish the cooling effect.

Figure 9(a) shows the height-averaged film Nusselt number distributions, $\overline{Nu}_f(Re_f)$, for different water inlet temperatures and wall heat fluxes. For comparison, the classical Nusselt correlation assuming $q_i = q_w$, i.e. conduction-dominated heat transfer, is included. For $T_r = 35°C$ and $q_w = 1$ kW m^{-2}, part of the heat source, q_w, is used to raise the liquid film temperature and hence the actual $\overline{Nu}_f(Re_f > 30)$ is higher than Nusselt's prediction. At $T_r = 50°C$, stronger interfacial blowing and increased gas flow rates result in significant gas phase cooling (cf. Fig. 9(b)) and therefore lower film Nusselt numbers. The gas-phase Nusselt number hardly increases with higher wall heat fluxes and hence $\bar{q}_i$ because the increase in buoyancy forces is not enough to offset q_w resulting in higher interfacial temperatures and therefore larger $\Delta T = \bar{T}_i - \bar{T}$ ($y = S$). In contrast, wider channels ($S = 0.02$ m) exhibit a higher gas-phase Nusselt number, $\overline{Nu}_g(S)$, because of the larger characteristic length used.

Table 3. Input data sets

$Pr_1 = 3.47$–4.87	$S = 0.01$–0.03 m
$Pr_2 = 0.7$–0.71	$H = 0.1$ m
$Sc_2 = 0.67$–0.68	$T_r = 35, 50°C$
$Gr_T = 1.83 \times 10^3$–4.96×10^4	$T_0 = 20°C$
$Gr_M = 4.36 \times 10^2$–1.17×10^4	$q_w = 1$–5 kW m^{-2}
$Re_f = 10$–200	$\phi_{H0} = 100\%$

Note: Fluid properties are evaluated at the reference temperature as follows: liquid film, $T_{ref} = T_r$ and gas flow, $T_{ref} = T_r - 1/3(T_r - T_0)$.

5. CONCLUSIONS

Transient and steady-state interactions of a falling liquid film, liquid evaporation and buoyancy-induced gas–vapor flow in a vertical finite channel with one heated wall have been analyzed for different film Reynolds numbers, wall heat fluxes, liquid inlet temperatures and channel aspect ratios. The following observations can be made and conclusions drawn from this study:

• The time-dependent developments of the gas–vapor flow field, due to drag-induced motion by the steady evaporating gravity film and natural convection caused by temperature gradients and concentration gradients, include in chronological order: simultaneous upward flow (upper channel half) and downward flow (lower channel half), vapor blowing at the interface, formation of a distinct recirculation zone along the gas–liquid interface, strong, steady drawdown of cool air by the falling film, as well as

the establishment of a buoyancy-driven gas–vapor flow and a (thin) recirculation layer along the interface.

- Mass diffusion due to vapor concentration gradients has a significant effect on the interfacial heat transfer. Specifically, such buoyancy-induced convection effects help to prevent high wall temperatures especially in the lower channel section.
- While relatively high film flow rates, $Re_f > 100$, can reduce the wall temperature, passive cooling with low film Reynolds numbers, $Re_f < 50$, can more effectively utilize film evaporation heat transfer. In general, the interfacial heat flux is predominantly determined by latent heat transfer rather than sensible heat transfer.
- Raising the water inlet temperature increases the buoyancy forces and the interfacial heat transfer causing only a moderate wall temperature increase over the film inlet temperature.
- As expected, larger wall heat fluxes not only decrease the relative interfacial heat transfer but also result in higher wall temperatures.
- Smaller channel widths cause larger buoyant gas flows which increase the heat transfer in the lower channel sections. However, the rapid increase in bulk temperature and vapor concentration decrease the interfacial heat transfer in the upper channel portion and hence may offset any gain.

In summary, the present study of combined falling liquid film and free gas convection heat/mass transfer in a vertical one-sided heated channel is a starting point for analysis and design applications in passive cooling of electronic equipment, manufacturing processes, (nuclear) reactors and natural phenomena. Future work should concentrate on the effects of liquid film wavy motions, turbulence and nucleate boiling as they apply to passive cooling systems.

REFERENCES

1. T. S. Chang and T. F. Lin, Transient buoyancy-induced flow through a heated, vertical channel of finite height, *Numer. Heat Transfer* **16,** 15–35 (1989).
2. E. M. Sparrow, G. M. Chrysler and L. F. Azevedo, Observed flow reversals and measured–predicted Nusselt number for natural convection in a one-sided heated vertical channel, *J. Heat Transfer* **106,** 325–332 (1984).
3. E. M. Sparrow and L. F. Azevedo, Vertical-channel natural convection spanning between the fully-developed limit and the single-plate boundary-layer limit, *Int. J. Heat Mass Transfer* **28,** 1847–1857 (1985).
4. C. J. Chang, T. F. Lin and W. M. Yan, Natural convection flows in a vertical, open tube resulting from combined buoyancy effects of thermal and mass diffusion, *Int. J. Heat Mass Transfer* **29,** 1543–1552 (1986).
5. B. Gebhart and L. Pera, The nature of vertical natural convection flows resulting from the combined buoyancy effects of thermal and mass diffusion, *Int. J. Heat Mass Transfer* **14,** 2025–2050 (1971).
6. F. K. Wasden and A. E. Dukler, Insights into the hydrodynamics of free falling wavy films, *A.I.Ch.E. Jl* **35**(2), 187–195 (1989).
7. N. Cerza and V. Sernas, Nucleate boiling in thermally developing and fully developed laminar falling water films, *J. Heat Transfer* **110,** 221–228 (1988).
8. R. S. R. Gorla and T. M. Maloney, Conjugate heat transfer in falling laminar liquid films, *Chem. Engng Commun.* **60,** 271–282 (1987).
9. G. Zabaras, A. E. Dukler and D. Moalem-Maron, Vertical upward concurrent gas–liquid annular flow, *A.I.Ch.E. Jl* **32**(5), 829–843 (1986).
10. T. Fujita and T. Ueda, Heat transfer to falling liquid films and film breakdown—I. Subcooled liquid film, *Int. J. Heat Mass Transfer* **21,** 97–108 (1978).
11. T. Ueda and H. Tanaka, Measurements of velocity, temperature and velocity fluctuation distributions in liquid films, *Int. J. Multiphase Flow* **2,** 261–272 (1975).
12. K. R. Chun and R. A. Seban, Heat transfer to evaporating liquid films, *J. Heat Transfer* **93,** 391–396 (1971).
13. T. F. Irvine, Jr. and P. E. Liley, *Steam and Gas Tables with Computer Equations*, pp. 21–24. Academic Press, New York (1983).
14. S. V. Patankar, *Numerical Heat Transfer and Fluid Flow*. McGraw-Hill, New York (1980).

ANALYSE DU REFROIDISSEMENT PASSIF DANS UN CANAL VERTICAL FINI UTILISANT UN FILM LIQUIDE TOMBANT ET UN ECOULEMENT GAZ–VAPEUR DE CONVECTION NATURELLE

Résumé—Une étudie fondamentale des effets couplés d'un film liquide tombant, avec vaporisation partielle, et d'un écoulement gaz–vapeur de convection naturelle dans un canal vertical chauffé sur une paroi est présentée pour différents nombres de Reynolds de film, plusieurs températures d'entrée du liquide, plusieurs flux thermiques pariétaux et espacements du canal. Les équations du transport variable (elliptique) de la phase gazeuse sont résolues numériquement en relation avec les équations du film liquide laminaire (parabolique). Le modèle de simulation numérique validé est utilisé pour dépeindre le développement variable des lignes de courant, des paramètres de la phase gazeuse et des grandeurs interfaciales aussi bien que les profils stationnaires de vitesse, de température et les distributions des nombres de Nusselt moyens. La présente analyse peut contribuer à la résolution des problèmes de refroidissement passif associés au fonctionnement d'équipement électronique, aux processus de fabrication à la conception des centrales nucléaires modernes et à de nombreux phénomènes d'environnement.

UNTERSUCHUNG DER PASSIVEN KÜHLUNG IN EINEM SENKRECHTEN ENDLICHEN KANAL MIT EINEM RIESELFILM UND EINER AUFTRIEBSGESTEUERTEN GAS–DAMPF-STRÖMUNG

Zusammenfassung—Die gekoppelten Effekte eines teilweise verdampfenden Rieselfilms und einer auftriebsinduzierten Gas–Dampf-Strömung in einem senkrechten einseitig beheizten Kanal wird grundlegend untersucht. Folgende Parameter werden variiert: Reynolds-Zahl des Filmes, Eintrittstemperatur des Filmes, Wärmestromdichte an der Wand und Weite des Kanals. Die transienten (elliptischen) Transportgleichungen für die Gasphase werden in Verbindung mit den (parabolischen) Gleichungen für den laminaren Flüssigkeitsfilm numerisch gelöst. Das validierte Simulationsmodell wird eingesetzt, um die transiente Entwicklung der Stromlinien, der Parameter für die Gasphase und der Schnittstellengrößen, wie auch stationäre Geschwindigkeitsprofile, Temperaturprofile und die Verteilung der gemittelten Nusselt-Zahl darzustellen. Die vorliegende Untersuchung mag zur Lösung von Problemen der passiven Kühlung beim Betrieb elektronischer Bauteile, bei Fertigungsvorgängen, bei der Auslegung moderner Kernkraftwerke und zahlreichen Umweltproblemen beitragen.

АНАЛИЗ ПАССИВНОГО ОХЛАЖДЕНИЯ В ВЕРТИКАЛЬНОМ КАНАЛЕ КОНЕЧНОЙ ДЛИЫ ПРИ ИСПОЛЬЗОВАНИИ СТЕКАЮЩЕЙ ЖИДКОЙ ПЛЕНКИ И СВОБОДНОКОНВЕКТИВНОГО ПОТОКА ПАРОГАЗОВОЙ СМЕСИ

Аннотация—Описывается фундаментальное исследование взаимосвязанных эффектов стекающей частично испаряющейся жидкой пленки и свободноконвективного паро–газового потока в вертикальном канале с односторонним нагревом при различных числах Рейнольдса пленки, температурах жидкой пленки на входе, тепловых потоках на стенке и параметров канала. Численно решаются сопряженные нестационарные уравнения переноса в газообразной фазе и уравнения для ламинарной жидкой пленки. Апробированная модель расчета на ЭВМ используется для описания нестационарных процессов обтекания и определения параметров газовой фазы и величин на межфазной границе, а также устойчивых профилей скоростей, профилей температур и распределений усредненных чисел Нуссельта. Предложенный анализ может успешно применяться для решения задач пассивного охлаждения, связанных с работой электронного оборудования, производственными процессами, современными конструкциями АЭС и различными явлениями, наблюдаемыми в окружающей среде.